

Failure Analysis of Dielectric Breakdowns in Base-Metal Electrode Multilayer Ceramic Capacitors

Ronald J. Weachock
Dell System Federal Government, Inc.
NASA Goddard Space Flight Center
Greenbelt, MD 20771
Ronald.j.weachock@nasa.gov

David (Donhang) Liu
MEI Technologies, Inc.
NASA Goddard Space Flight Center
Greenbelt, MD 20771
Donhang.liu-1@nasa.gov

Abstract

Leakage current measurements of BaTiO₃-based X7R multilayer ceramic capacitors (MLCCs) with base-metal electrodes (BMEs) have revealed three distinct failure modes: avalanche breakdown (ABD), thermal runaway (TRA), and slow degradation. Failure analysis (FA) was performed for a number of BME capacitors that failed with the aforementioned three failure modes. The samples that failed with ABD had damage sites that were easily found and that were characterized by the existence of incompletely burned binder particles that were surrounded by transverse cracks that extended through several layers of electrodes from the damaged site, clearly a sequence caused by thermal damage. The samples that failed with TRA also had a particle-like processing flaw with high carbon content, but the flaw was smaller than that of the ABD failure samples. The failure site was also surrounded with extensive transverse cracks that extended through many dielectric layers. Degraded dielectric and conglomerates of nickel spheres were also revealed, indicating a severe thermal event that generated excessive heat and that resulted in the melting of the local dielectric and electrodes. There is no fundamental physical difference between ABD and TRA failures for BME capacitors. The failure mode is a combination of ABD and TRA and is referred to as “catastrophic.”

The failure analysis on the samples that failed with a slow degradation indicates a failure process that can be described as follows: The electromigration of oxygen vacancies not only gives rise to a gradual increase of leakage current against stress time, but also changes the initial stoichiometry of BaTiO₃ grains and causes the local hollowing and melting of dielectric grains and the formation of cracks. The molten dielectric dissolves the internal nickel electrodes and transports the nickel along the transverse cracks, which causes the resistive short. Some of the cracks with dielectric degradation will eventually result in a catastrophic failure. The failure process involves a localized high temperature that can melt both dielectric and nickel. There was no evidence of nickel migration in the BME capacitors, even under highly accelerated life stress conditions.

The failure analysis indicates that failure mechanism in BME capacitors with BaTiO₃ dielectrics can be more accurately described as a two-stage dielectric wearout that begins with a slow dielectric degradation, characterized by a gradual increase in leakage current with stress time, and followed by a thermally dominated catastrophic breakdown (either ABD or TRA).

Introduction

Three distinct failure modes were revealed from time-dependent dielectric breakdown leakage current measurements of BaTiO₃-based X7R multilayer ceramic capacitors with base-metal electrodes (BMEs): the so-called avalanche breakdown (ABD), thermal runaway (TRA), and slow degradation. The measurements were performed by collecting leakage current data as a function of stress time during highly accelerated life stress testing (HALST). This study was conducted in order to evaluate the reliability of BME capacitors and access their suitability for space flight applications [1].

The concepts of ABD and TRA were first introduced for describing failure modes for ceramic capacitors with precious-metal electrodes (PMEs) as early as 1984 [2].

ABD failures are normally caused by extrinsic defects within the dielectric, such as cracks, voids, or other pre-existing processing flaws. ABD observed in semiconductor devices is typically a purely chain-reaction electronic process that will cause a sudden, catastrophic breakdown in which the temperature rise is almost negligible [3]. When the leakage current was recorded against time, it was found that the ABD can occur at extremely low leakage current levels and that the time from the onset of breakdown to the final catastrophic burning of the device is in the range of nano- to micro-seconds for semiconductor devices. However, this time measurement for most of the BME capacitors with ABD-like failures was often in milliseconds or even longer [1].

TRA failures are usually caused by intrinsic defects that represent the inhomogeneity in the dielectric composition or microstructure, or even in the morphology. When a DC voltage is applied, the intrinsic defects will often cause a local increase of current and therefore an increasing localized temperature. Since for most oxide-based dielectrics the leakage current increases with temperature, a local increase of temperature will result in an increase of current and will cause a further temperature increase. As a result, a positive feedback loop is formed that will eventually cause the thermal breakdown of the dielectric. An example of a microstructure anomaly which could cause a TRA failure is the over-firing of the dielectric, resulting in the formation of a low-resistance BaTiO₃ grain [4].

Slow degradation failures are characterized by a gradual increase of leakage current against stress time until a failure criterion is reached (100μA in this study). This failure mode is unique for BME capacitors that normally were sintered in a reducing atmosphere and resulted in a high concentration of oxygen vacancies. The degradation under a DC field involves electromigration and accumulation of oxygen vacancies across the dielectric layers towards the cathode. There is also a pileup of oxygen vacancy at the cathode side of the grain and within each BaTiO₃ grain, which results in BaTiO₃ grains becoming locally more conductive [5,6].

Four BME capacitors that failed during HALST with the aforementioned three failure modes were selected and processed for failure analysis. The objective was to reveal possible correlations between dielectric breakdown failure modes and the physical characteristics at the failure sites. All FA samples were from the same manufacturer lot and had the same product part number. Two of the capacitors had ABD failures, one had a TRA failure, and the fourth failed with a slow degradation.

Construction Analysis and HALST Testing of BME Capacitors for Failure Analysis

Commercial BME capacitors from manufacturer B with a designated part number of B08X56416 were selected for construction analysis prior to the HALST. The capacitor is 0.56μF and 16V, with an EIA chip size of 0805, and was made with a BaTiO₃-based X7R dielectric.

Five as-received fresh BME capacitors from the same production lot were cross-sectioned for optical scanning electron microscope (SEM) and energy-dispersive X-ray (EDX) inspection to check for possible extrinsic processing defects such as cracks, voids, or delamination. The capacitor samples were etched with diluted Hydrogen Fluoride (HF) for the purpose of delineating details on the construction of the capacitor, the dielectric microstructure, and the possible existence of cracks in the dielectric layers before the SEM and EDX examinations.

Figure 1 shows the low-magnification SEM images that have been used to determine the capacitor geometry and the overall quality of the product. The cross-section SEM images reveal a uniform structure without obvious processing flaws, with the exception of some internal electrode pull-out caused by the de-processing of the samples. The construction information was examined according to Electronic Industries Alliance (EIA) Standard EIA-496.

Typical high-magnification SEM images are shown in Figure 2. The dielectric layer appears to be dense and uniform, with an average layer thickness of 4.2μm and an average grain size of 0.36μm, with a maximum of 0.4μm measured. No dielectric cracks, either long-range or short-range, were observed in any of the samples. Some minor voids could be observed in the dielectric matrix (indicated by arrows).

Table I summarizes construction and microstructure information for this BME product. The reliability figure of merit was evaluated using an empirical formula that was developed earlier for screening commercial BME capacitors for high-reliability applications [7]:

$$R(t < \eta) = \left[1 - \left(\frac{r}{d} \right)^\alpha \right]^N, \quad (1)$$

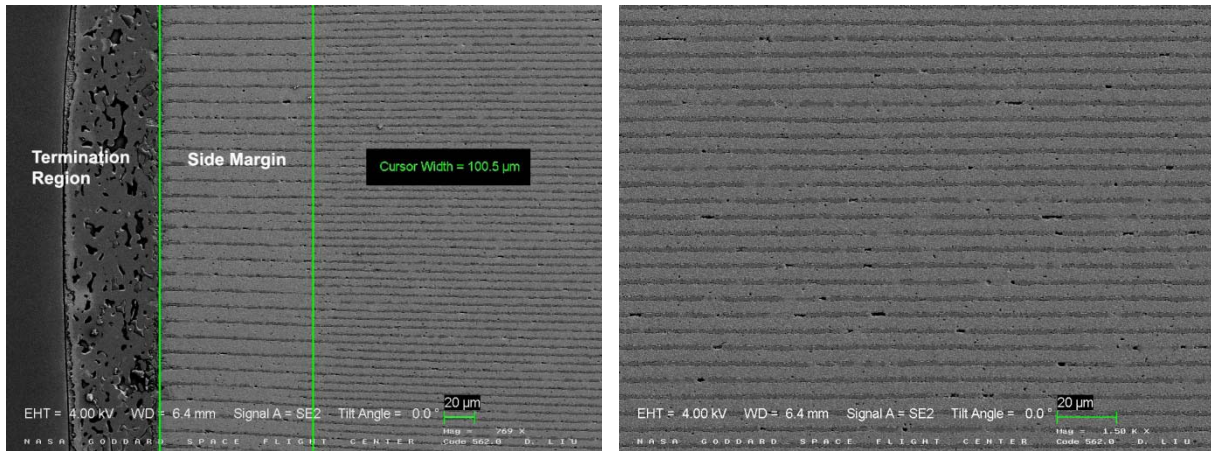


Figure 1. Low-magnification cross-section SEM images of BME capacitor B08X56416 for construction analysis. No processing flaws were revealed, with the exception of some internal pull-out due to sample de-processing.

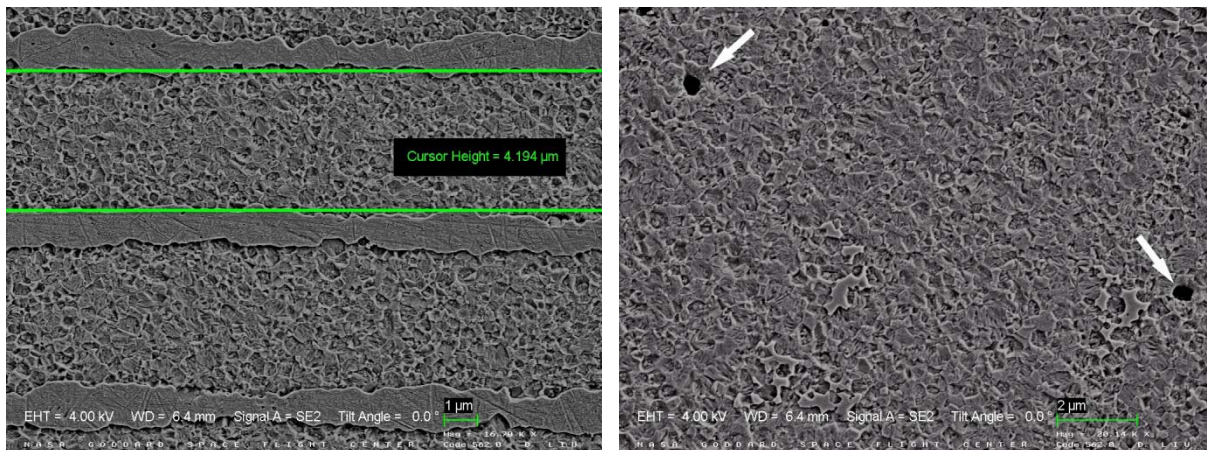


Figure 2. High-magnification cross-section SEM images of BME capacitor B08X56416 reveal a uniform microstructure. Arrows indicate occasionally observed voids in the dielectric.

In this equation, d is the average dielectric thickness, \bar{r} is the average grain size that is equal or smaller than d , N is the total number of dielectric layers, and α is the empirical parameter that typically equals 6. The calculated value of $R(t < \eta) = 99.994\%$ from Eq.(1) indicates this BME product is acceptable for high reliability applications [7].

Table I. Information on the construction and microstructure of the BME capacitor from this study

Capacitor ID	Construction Information			
	End Margin	Side Margin	Cover Plate	No. of Dielectric Layers
B08X56416	170 μm	100 μm	365 μm	82
Microstructure Information				
Capacitor ID	Dielectric Thickness	Avg./Max. Grain Size	No. of Grain Stacking	$\left[1 - \left(\frac{\bar{r}}{d}\right)^\alpha\right]^N$
B08X56416	4.2 μm	0.36 μm /0.4 μm	11.67	99.994%

The as-received BME capacitor B08X56416 was mounted on a custom printed circuit board (PCB) for HALST testing under various accelerated voltage and temperature combinations. The leakage current as a function of stress time was also monitored and recorded for the purpose of determining the failure modes. In this study, the failure criterion was set such that a BME capacitor will be considered a failure if its leakage current reaches 100 μA . Figure 3 shows typical leakage current measurement results of BME capacitors after HALST. Three failure modes as

described in this report are also illustrated. Details on the procedure of proposed HALST method has been described in reference [1].

Table II summarizes the HALST conditions and corresponding failure modes with respect to those shown in Figure 3. The DC resistance of the failed BME capacitors was also measured prior to sample preparation for failure analysis. In general, the parts with TRA and slow degradation failures showed low resistance with an occasional short, and those that failed with ABD often failed with an electric short.

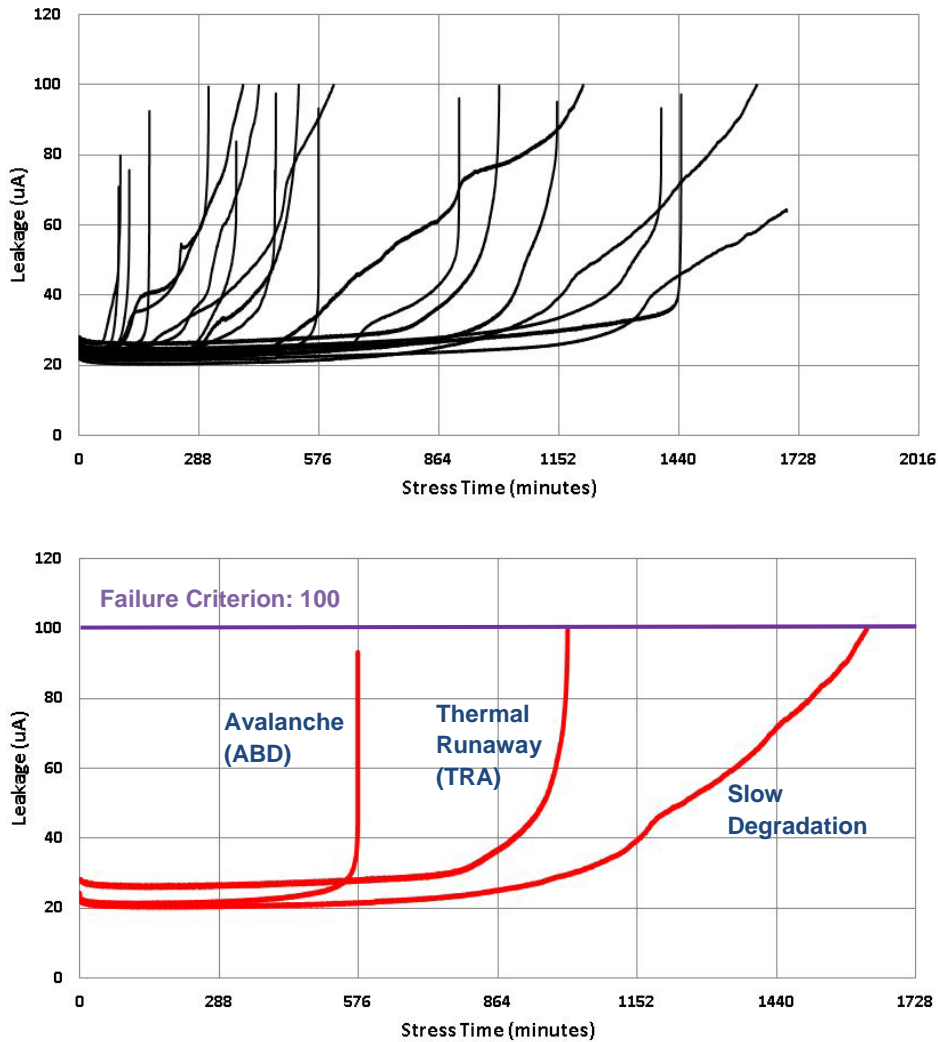


Figure 3. Three distinguishable failure modes observed in a typical leakage current measurement of BME capacitors.

Results of Failure Analysis

During FA sample preparation, the electrically failed BME capacitors were mounted on test fixtures that allowed electrical access to the end termination through wire contacts. The test fixture supporting each capacitor was positioned in an epoxy mounting cup to allow the alternately stacked layers of electrodes to be exposed by sequential de-layering of the sample and exposure of a vertical multilayer cross-sectional view of the dielectric and electrodes. Preparation of the fixture in this manner also allowed continuous monitoring of the capacitors’ resistance value as the capacitors were meticulously de-processed.

Table II. HALST Test conditions and failure modes of FA samples in this investigation

Number	HALST Test Conditions	Failure modes	Resistance (Ω)
SN1	155°C/140V	Avalanche (ABD)	<0.1
SN2	155°C /140V	Slow Degradation	960
SN3	165°C /180V	Avalanche (ABD)	<0.1
SN4	175°C /140V	Thermal Runaway (TRA)	245

1. BME Capacitors That Failed with ABD

Optical images of sample SN1 before and after etch are shown in Figure 4. A damaged failure site was easily located. The etched image clearly delineates the long-range cracks that cross several dielectric layers, offshoot from the damage site. A high-magnification SEM image and corresponding EDX mapping result are shown in Figure 5. A high concentration of carbon was identified inside the failure site, and the carbon distribution was not uniform. Since no carbon-containing material (including polish media) was used in de-processing the FA samples, the localized carbon residuals detected by EDX scan are likely from the binder particles that were introduced during the dielectric sheet casting.

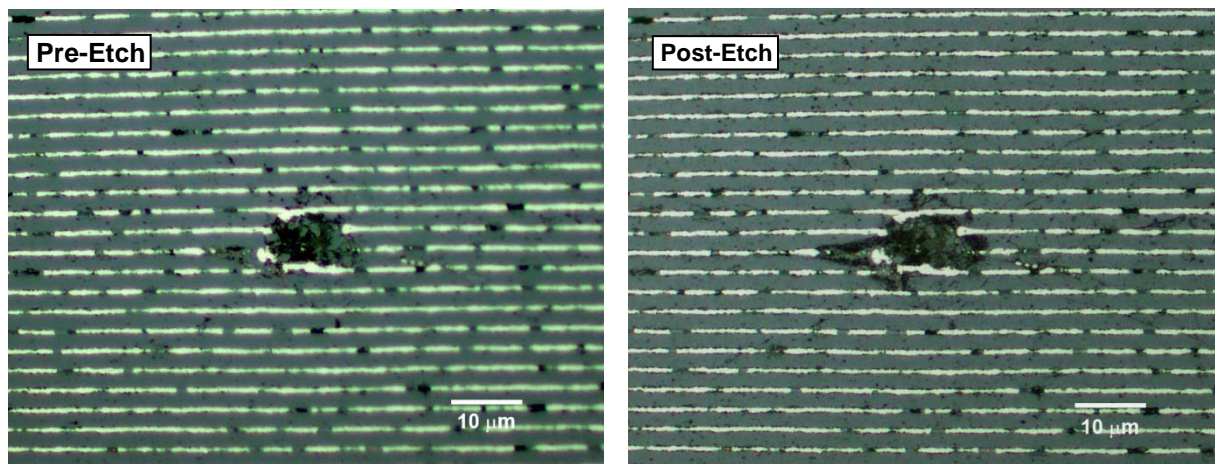


Figure 4. Optical images for SN1 before and after etch. A significant number of cracks are delineated in the etched image.

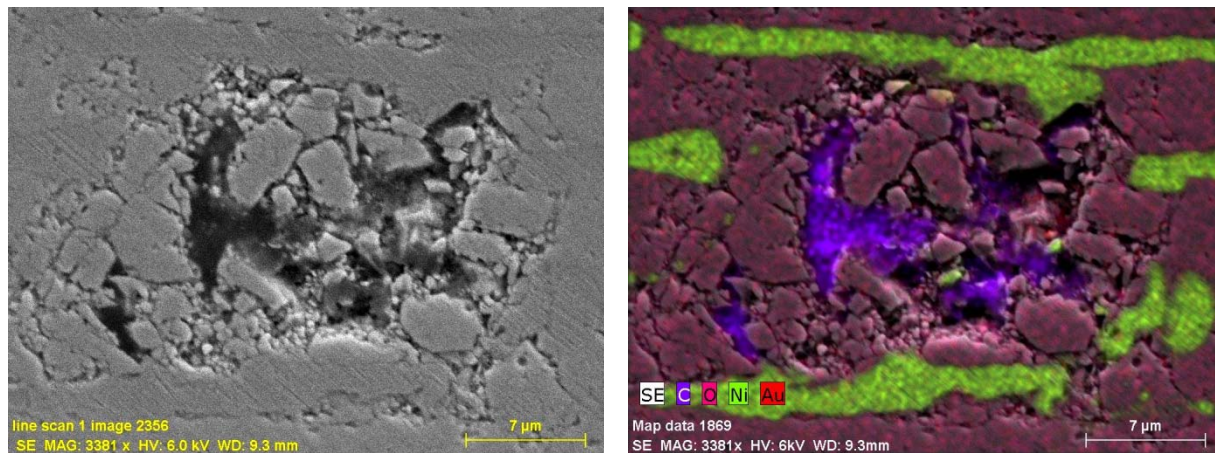


Figure 5. High-magnification SEM photo and corresponding EDX map of the damage site in SN1. EDX mapping of the area shows a high concentration of carbon within.

Figure 6 shows SEM images of the post-etched surface morphology of SN1. Arrows indicate the nickel spheres at the damage site that are distributed inside a transverse dielectric crack. This observation strongly supports the assumption that SN1 experienced a high-temperature thermal event that resulted in the melting and recrystallization

of internal nickel electrode material. Since the sample was identified as an ABD failure in the leakage current measurement, the results shown in Figure 6 suggest that even during an ABD process, a thermal event characterized by molten nickel spheres also occurred.

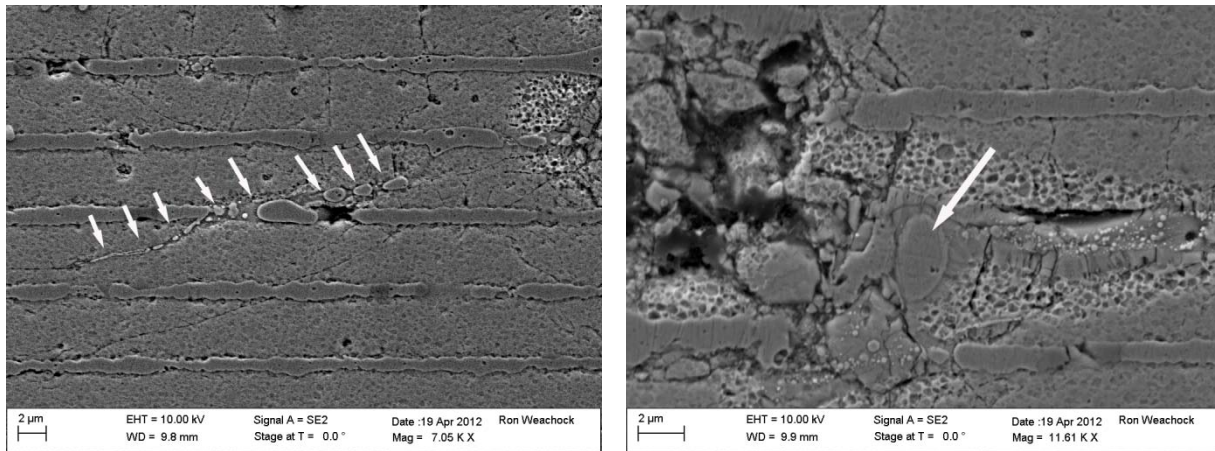


Figure 6. High-magnification SEM photos of SN1 near the damage site. Arrows indicate the conglomerates of Ni spheres distributed at the damage site and inside a transverse crack.

High-magnification SEM image and a corresponding EDX map of ABD-failed SN3 are shown in Figure 7. The size and morphology of the damage site look similar to that of SN1 (shown in Figure 5). Non-uniformly distributed carbon was also identified at the failure site. Figure 8 shows SEM images of the post-etched surface morphology for SN3. Arrows indicate the nickel spheres at the damage site and distributed inside a transverse dielectric crack.

It is very clear that the ABD failures observed in both SN1 and SN3 may have shared the same failure mechanism: incompletely burned carbon binder residuals that behave as extrinsic defects. In addition, although both samples are characterized as ABD failures, the FA results clearly showed evidence that a high-temperature event also occurred and caused typical thermal damages in both FA samples.

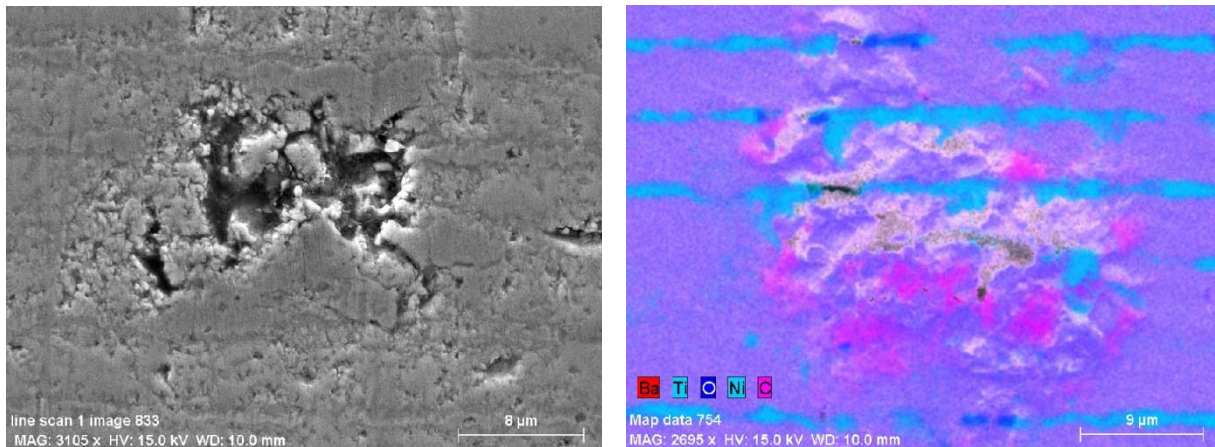


Figure 7. High-magnification SEM photo and corresponding EDX map of the damage site in SN3. EDX mapping of the area shows a high concentration of carbon at the damage site.

2. BME Capacitors That Failed with TRA

Capacitor SN4 was found to have failed with a resistive short that measured 245Ω. SN4 showed a constant resistance value as the de-processing analysis progressed through the capacitor. An infrared (IR) camera was used to isolate the area of interest. The resultant IR temperature imaging showed the location of the shorted area. A typical IR image that created a visible hot spot at ~4V and ~6mA, and a corresponding optical image identifying the failure site and a long-range crack that traveled through several dielectric layers are shown in Figure 9.

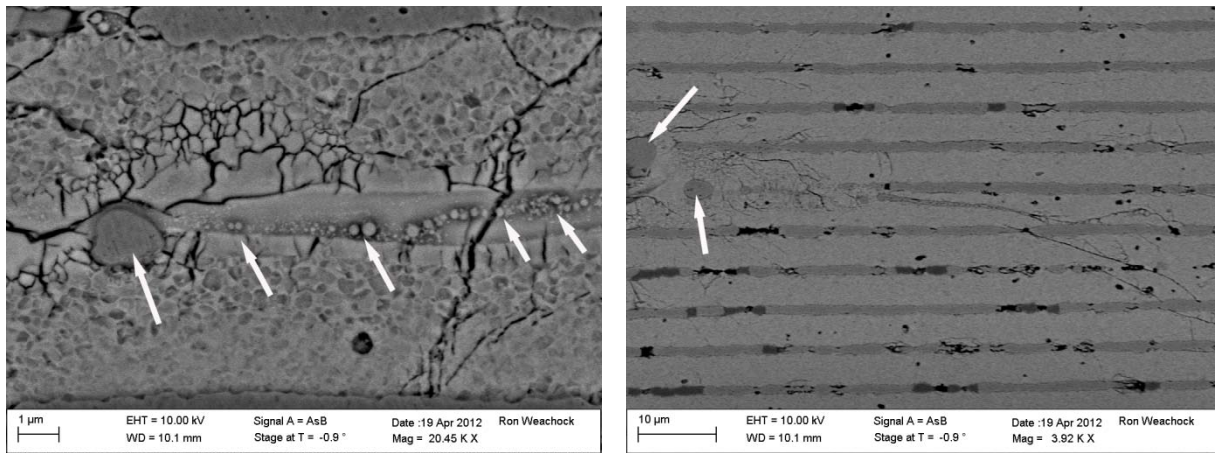


Figure 8. High-magnification SEM photos near the damage site. Arrows indicate the conglomerates of Ni spheres distributed at the damage site and inside a transverse crack.

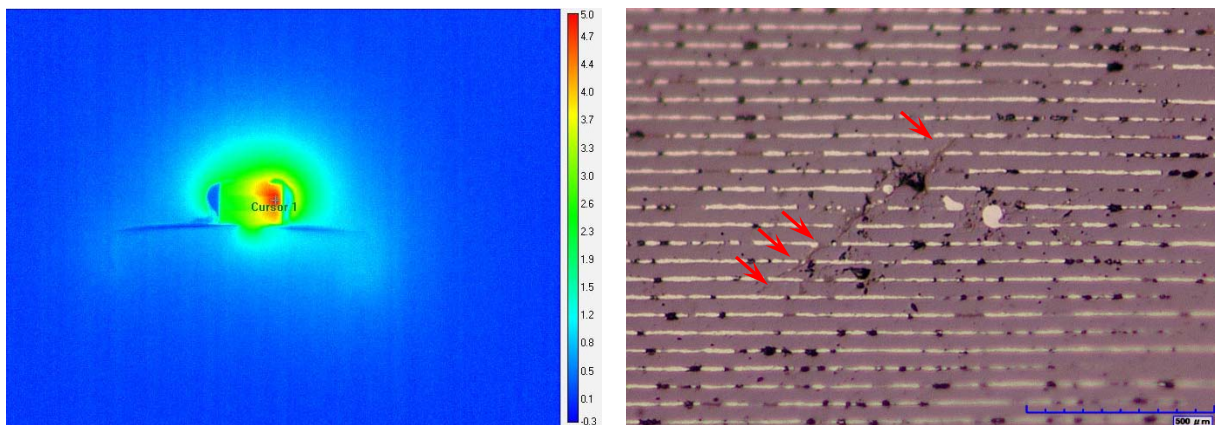


Figure 9. An IR camera image was used to localize the hot spot in SN4 by analyzing the temperature gradient of the heat dissipated by the short (left). The corresponding optical image shows the region isolated by IR images for which a thermal gradient between opposing electrodes, corresponding to vertical shorts between electrodes, was detected. The red arrows indicate the transverse crack (right).

A high-magnification SEM photo and corresponding EDX map of the damage site are shown in Figure 10. The failure site morphology looks similar to that observed for SN1 (Figure 5) and for SN3 (Figure 7), but with a smaller feature size. Again, a localized high carbon concentration and the formation of nickel spheres were both revealed.

Figure 11 shows SEM images of an area close to the damage site. To better reveal the details of the area, both secondary electron mode (electrons show topography of a sample) and backscatter mode (contrast is due to the difference in the atomic numbers of the materials) SEM images were taken. It is interesting to note that at the lower left corner, a pool of molten material was formed inside an extensive crack, and the conglomerates of a number of nickel spheres are distributed in the molten material. Although the morphology shown in Figure 11 is very similar to that shown in Figures 6 and 8 for the ABD failures, the transverse crack found in SN4 appears to be more extensive, indicating that this sample might have experienced a longer and more intense high-temperature event prior to failing.

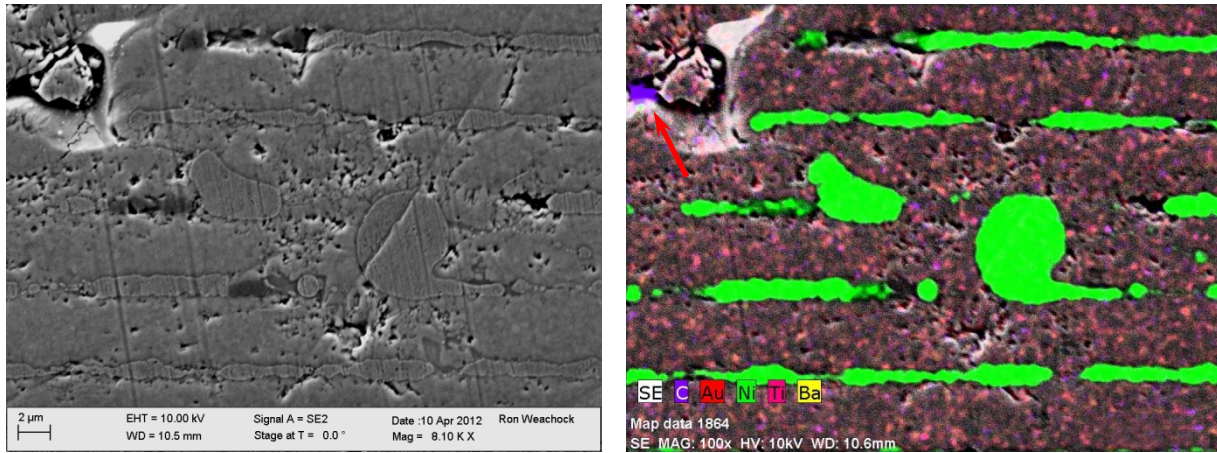


Figure 10. High-magnification SEM photo and corresponding EDX map of the damage site in SN4. Arrow in EDX map of the area indicates the high carbon concentration spot. The molten Ni spheres can be clearly identified.

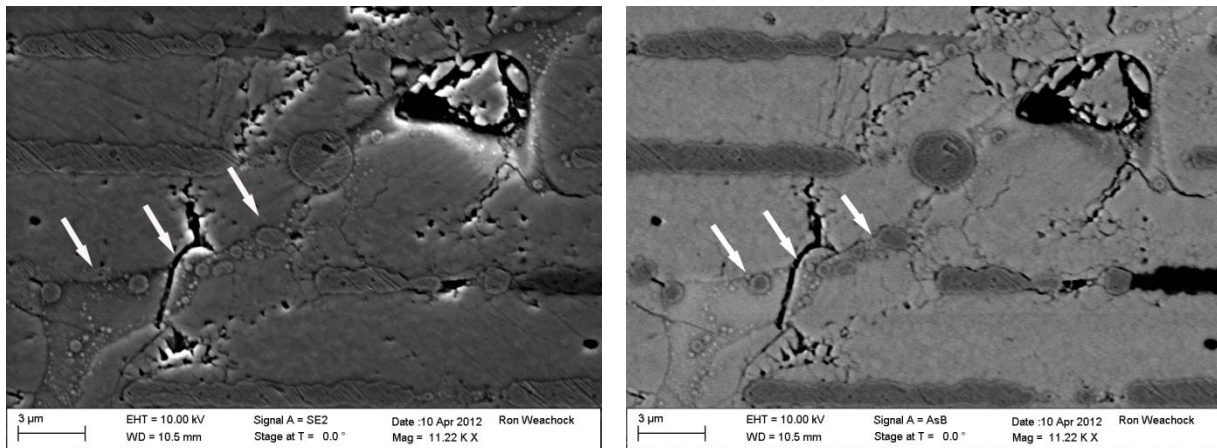


Figure 11. SEM images of an area close to the damage site. The left SEM photo was taken in secondary electron mode, and the right photo was taken in backscatter mode. An extensive crack filled with a molten material can be seen at the lower left corner of the image. Arrows indicate the Ni spheres distributed inside the pool.

3. BME Capacitors That Failed with Slow Degradation

BME capacitor sample SN2, which failed in slow degradation mode, was carefully de-processed using numerous iterations of the steps for material removal. Resistance measurements were taken after each polishing interval to determine whether resistance changes were experienced during the destructive process that could indicate that the defect site had been reached or was in the process of being exposed. The initial resistance was 960Ω and did not change during the material removal process. To assist with the identification of the failure site, an IR camera was used again as 4V was applied and 4mA was measured to the sample to show the temperature elevation in the damaged area and to allow the camera to obtain IR thermograph images and delineate a thermal site of interest. Figure 12 shows the IR optical images that reveal the failure site.

Figure 13 shows an SEM image and corresponding EDX map of the crack area identified in Figure 12. The result clearly shows a nickel bridging crossing several dielectric layers, and this is believed to be the cause of the low resistance measured in the sample. However, it is not clear why such a nickel bridging did not result in a complete electrical short.

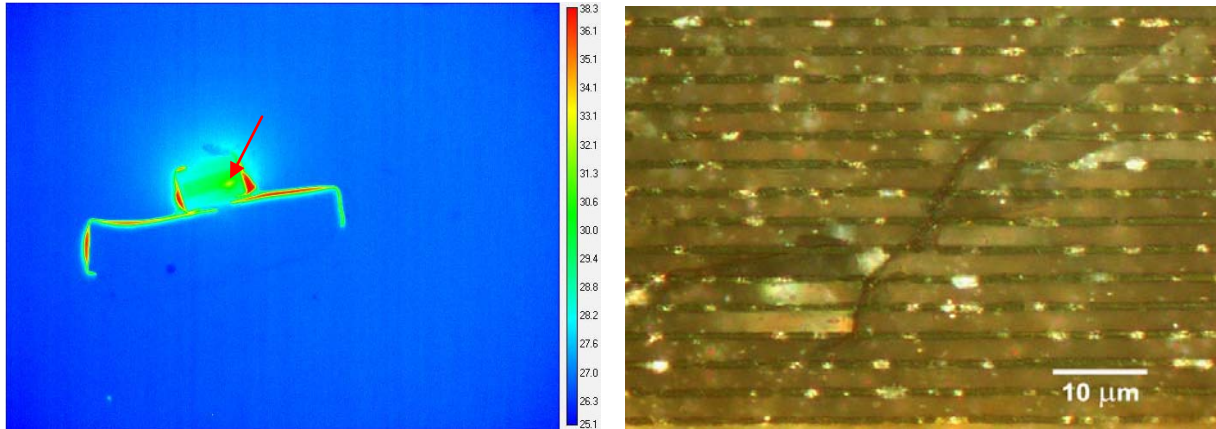


Figure 12. SN2, which maintained a stable resistive short throughout the analysis, was analyzed using an IR camera to localize the hot spot at ~4V, 4mA (left). Physical verification of the IR imaging hot spot location showed vertical dielectric cracks crossing several internal electrode layers (right).

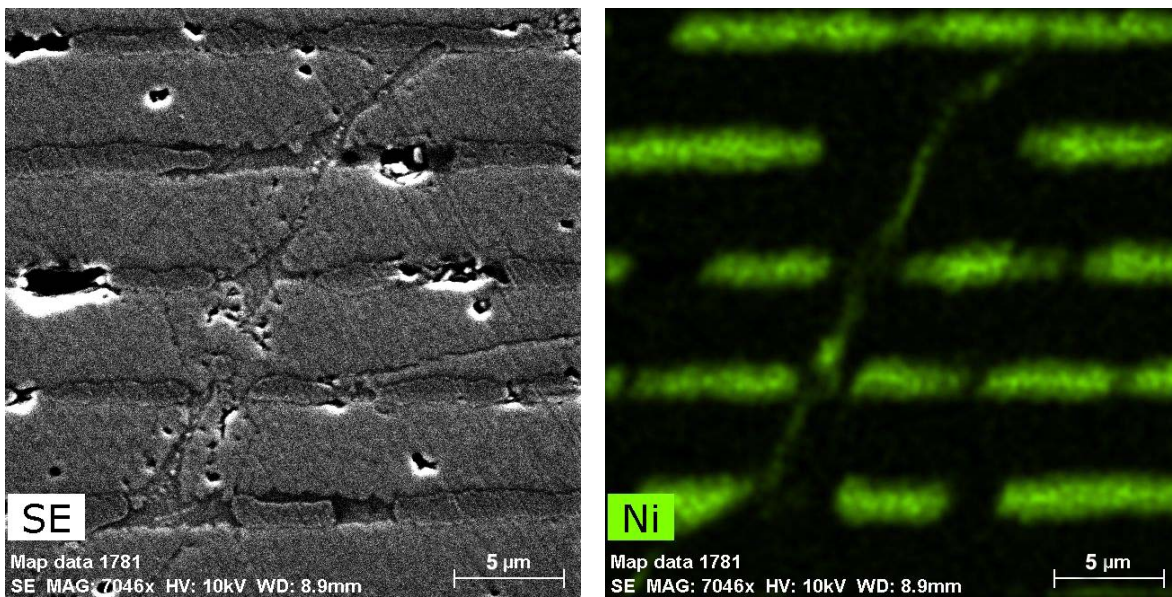


Figure 13. High-magnification SEM photo of one region of a large transverse crack crossing several internal electrodes (left). Photo on the right is the corresponding EDS map, showing nickel bridging.

To better understand the failure mechanism in SN2, the area was etched with dilute HF in order to delineate the morphological details. Figure 14 shows SEM images of the same area post-etch. The extensive transverse crack was backfilled with a molten material with a conglomeration of nickel spheres of various sizes. Some hollows in the dielectric region can be observed near the crack. The morphology is clearly a consequence of thermal damage that occurred during the accelerated life stress testing.

Figure 15 shows a void region when the sample was further de-processed for material removal. The void measured ~25μm long by 8.4μm wide and transverses several dielectric layers. Horizontal and vertical cracks propagate from the void region. Conglomerations of nickel spheres (indicated by arrows and confirmed by EDX mapping) are present in and around the void.

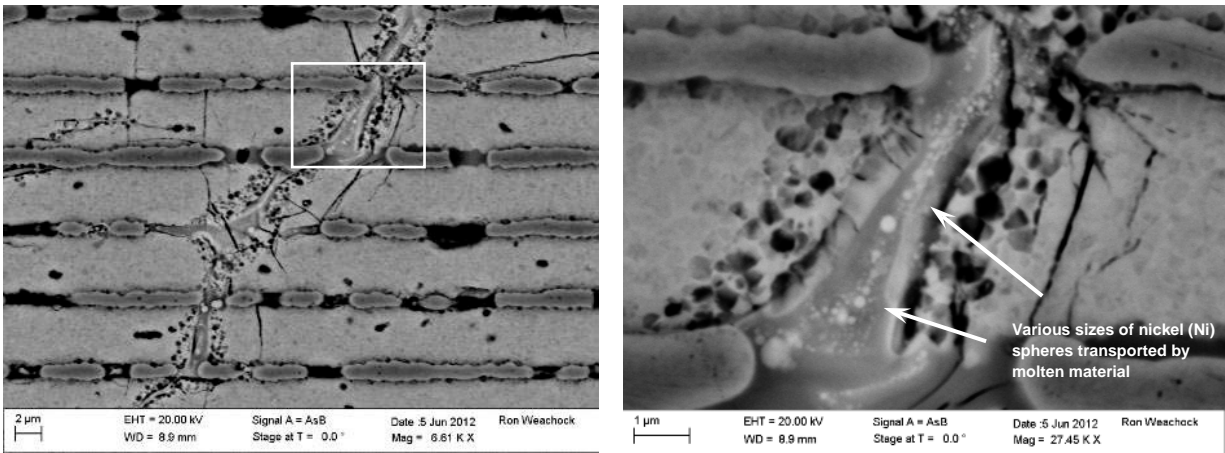


Figure 14. High-magnification SEM photo of the same region shown in Figure 13 after dilute acid etch. The transverse crack contains amorphous-looking material that once appeared to be molten and that acted as a vehicle for transporting nickel spheres of various sizes across opposing electrodes.

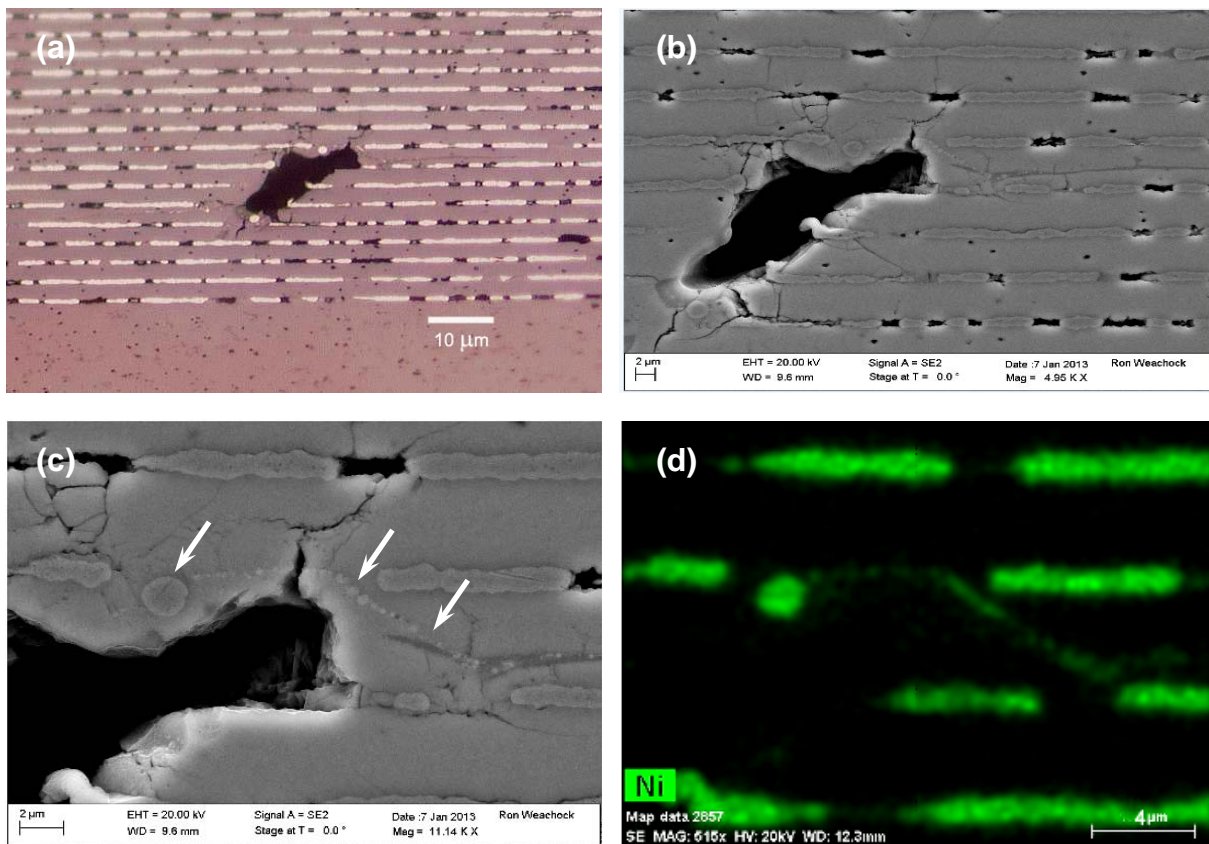


Figure 15. Optical image (a) and corresponding SEM image (b) of a void region due to dielectric degradation caused by localized heating. High-magnification SEM image (c), showing an intermediate cross-sectional plane with accumulation of nickel spheres within the dielectric layer that was confirmed by EDX mapping (d).

Figure 16 shows SEM images of the void region post-HF etch. The dielectric morphology is delineated and better characterized. Two different types of cracks were revealed: (1) cracks with dielectric degradation that are surrounded by hollow BaTiO₃ grains, and (2) regular stress cracks without dielectric degradation.

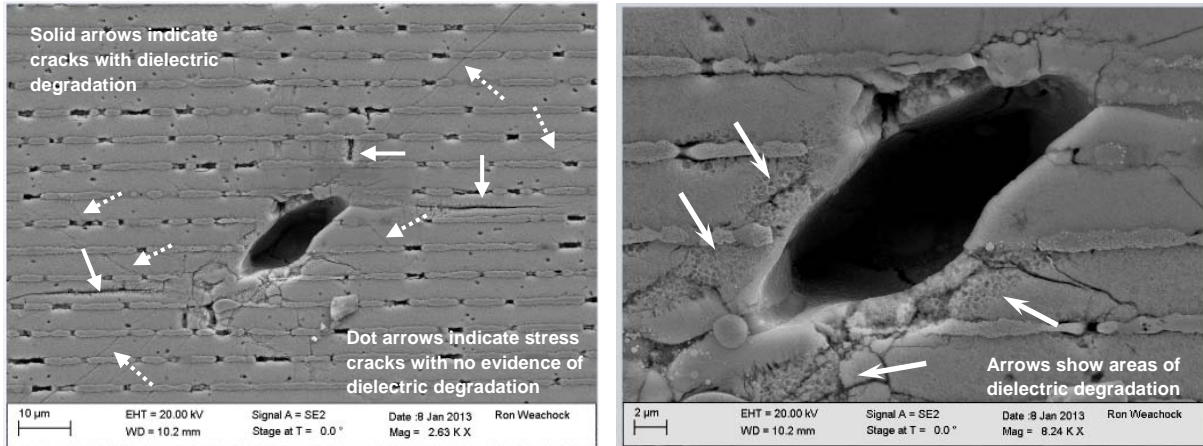


Figure 16. SEM images of void dielectric morphology post-acid etch reveal two types of cracks: cracks with dielectric degradation (indicated by solid arrows), and regular stress cracks (indicated by dotted arrows).

Figure 17 shows SEM images of the void region and the approaching void bottom after several iterations of further material removal. The images were taken after the area was etched to expose possible new evidence of secondary defects. The void walls were covered with a thin layer of amorphous-looking molten material. The large nickel spheres were present in and around the wall, which is apparently the consequence of nickel segregation and recrystallization after temperature had cooled off. There is no other explanation for how such big nickel spheres could be formed.

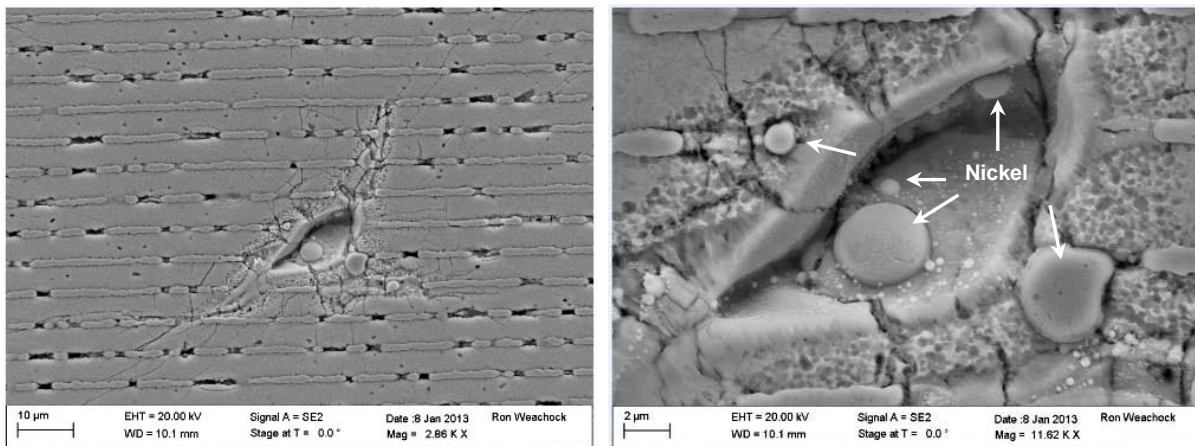


Figure 17. SEM images of void region after etch. Pools of nickel and degradation of the dielectric are shown. The internal surface area of the void was not affected by acid etch.

Figure 18 shows SEM images of a cross-section plane beyond the void region. An extensive long-range crack with dielectric degradation was revealed. Two selected areas were examined with high-magnification SEM. The results show: (1) nickel conglomerates can only be found in cracks with dielectric degradation; (2) no trace of nickels are found in stress cracks; (3) nickel spheres are always distributed on the surface of the molten dielectric, and (4) the molten dielectric is always surrounded by hollow BaTiO₃ grains that are formed by thermal degradation.

Figure 19 shows SEM images of the damage area post-etch that appears to be in the initial stage of a dielectric degradation. A needle-like molten dielectric material is bridging the adjacent nickel electrodes and is fully in contact with the neighboring nickel material (as indicated by arrows). The molten material is surrounded by hollow BaTiO₃ grains. The corresponding EDX map shows that the bridging material contains only Ba, Ti, and O. There is no evidence of the presence of nickel in the molten material.

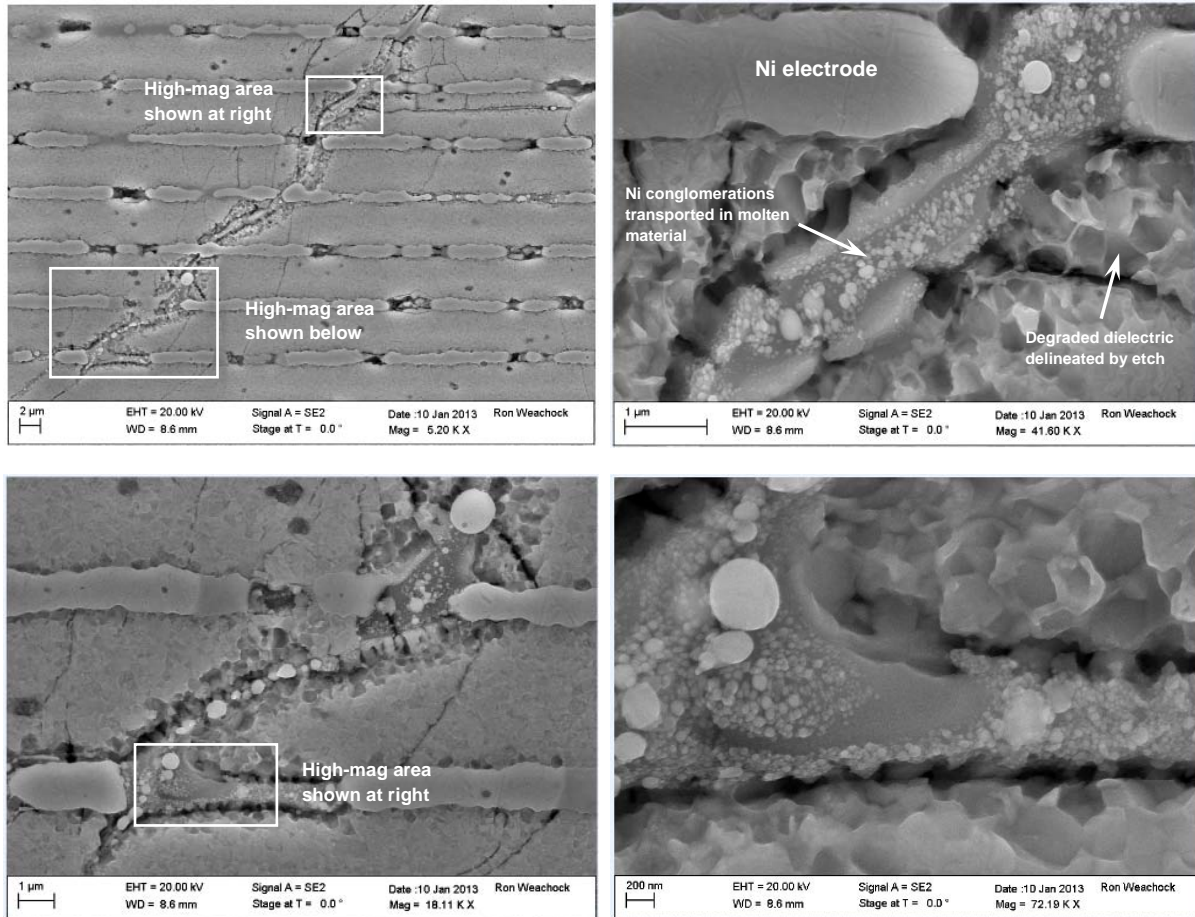


Figure 18. SEM images, showing post-etch dielectric cracks and degradation beyond the void region. Ni sphere conglomerations always were found to be distributed on the surface of the molten dielectric and to be surrounded by degraded BaTiO₃ grains.

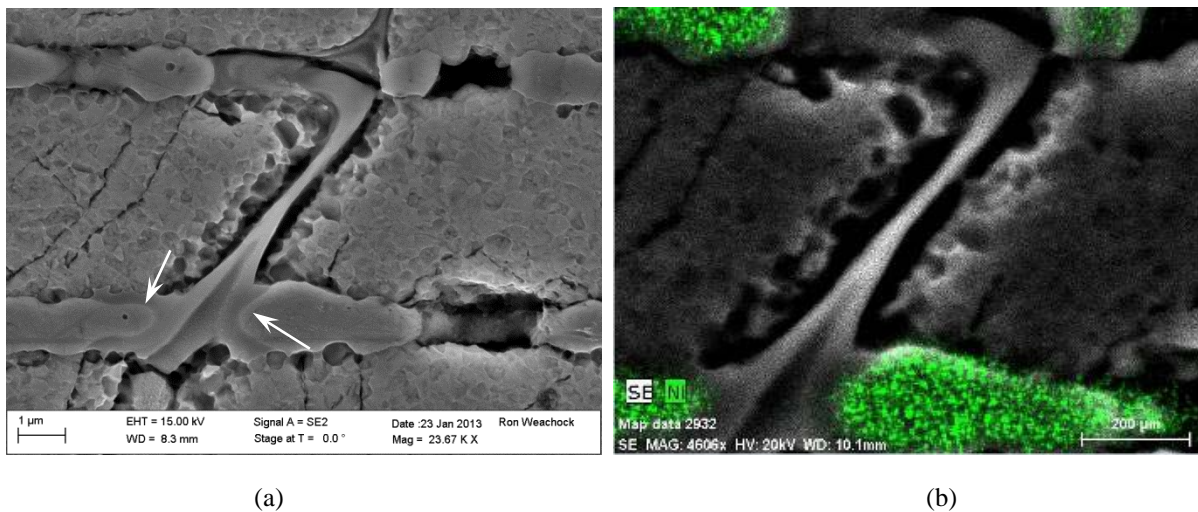


Figure 19. SEM image (a) shows post-etch dielectric crack and what appears to be initial-stage degradation. The corresponding EDX map (b) did not reveal any nickel in the crack. However, the nickel electrode is fully surrounded by the molten dielectric (indicated by arrows).

This observation indicates that dielectric degradation began with the melting and traveling of dielectric materials along the cracks. When the molten dielectric was in contact with the nickel electrode, the nickel began to dissolve into the molten dielectric, and the molten dielectric behaved as a vehicle for transporting the dissolving nickel along the transverse cracks, which resulted in an electrical short. However, after the temperature had cooled off, the dissolved nickel segregated from the molten dielectric and solidified on the surface of molten dielectric to form conglomerates of nickel spheres. This observation clearly indicates that there was no nickel migration in the BME capacitors, even under highly accelerated life stress conditions being used in this study.

This explains why nickel on the surface of molten dielectric never forms a uniform, continuous conduction phase and why no trace of nickel was found in any of the stress cracks that do not have dielectric degradation. The conducting chain that bridges the internal electrode layers was formed by the neck-to-neck connection among the conglomerated nickel spheres, and therefore it only exhibited low resistance, but not a complete electrical short.

Discussions

1. Avalanche and Thermal Runaway Failures

As pointed out earlier, the ABD failure is a purely electronic process in which the rise of the crystal lattice (phonon) temperature is normally negligible [3, 8]. ABD failures in SN1 and SN3 had easily identifiable damage sites, characterized by the existence of incompletely burned carbon binder particles, and surrounded by a significant number of cracks with dielectric degradation and stress cracks without dielectric degradation. These cracks offshoot several dielectric layers from the damage site, clearly a consequence of thermal damage.

SN4, which failed with TRA, revealed a local hot spot when an IR camera was used to map the temperature distribution in the ceramic body. A high carbon containing spot was also identified at the damage site, but it was much smaller in size when compared to that found in SN1 and SN3 for ABD failures. The failure site was also surrounded with extensive transverse cracks that traveled through many layers of internal nickel electrodes. Degraded dielectric and conglomerates of nickel spheres were also revealed, which is a typical result from a thermal event that generated heat high enough to melt both the local dielectric and the electrodes.

The ABD and TRA failure modes have been proposed and applied to describe the different features of dielectric breakdown in SiO₂ gate dioxide [8]. The TRA was also applied to explain the junction breakdown in bipolar devices. Both ABD and TRA failures can be clearly separated and modeled for SiO₂ materials [9]. However, the similarity in physical characteristics among SN1, SN3, and SN4 indicates that there is no observed fundamental physical difference between ABD and TRA failures for these BME capacitors. The failure mode in these BME capacitors can be viewed as a combination of both ABD and TRA. The reason for this is that the thermal conductivity of SiO₂ is at least 50 times higher than that of ceramic BaTiO₃, and the thermal diffusivity of SiO₂ is ~78 times higher than that of ceramic BaTiO₃. The relatively poor thermal properties of BaTiO₃ are the true reason that makes ABD failures more thermal runaway-like and TRA failures more avalanche-like in BME capacitors with BaTiO₃ dielectric. As a result, the ABD and TRA failures shown in Figure 3 were often found to be experimentally indistinguishable for BME capacitors. Both of these failure types are generally referred to as “catastrophic” failures.

In a previous report, an effort was made to separate ABD and TRA failures using measured leakage current data in order to better understand the failure mechanisms in BME capacitors [10]. However, as more experimental leakage current data were presented and analyzed, the difference between ABD and TRA failures appears to be virtually indistinguishable. The similar failure mechanism for ABD and TRA that is revealed in the present study confirms this previous hypothesis.

2. A Two-Stage Dielectric Wearout in BME Capacitors

The failure analysis results shown in Figures 18 and 19 indicate that slow degradation begins with the electromigration of ionized oxygen vacancies that changes the local stoichiometry of BaTiO₃ grains and causes the local hollowing and melting of BaTiO₃ grains and the formation of cracks. The molten dielectric dissolves the internal nickel electrodes and behaves like a vehicle for transporting the nickel along the transverse cracks and results in a reduction in resistance. Some of the cracks with dielectric degradation will eventually result in a catastrophic failure.

Another issue with respect to the molten dielectric in slow degradation failures was brought up by this study: The local temperature for a slow degradation failure must be at least as high as the melting point of nickel (1455°C), so

that nickel electrodes can be molten and transported with the melting dielectric material. The melting temperature of BaTiO_3 is $\sim 1612^\circ\text{C}$, according to the phase diagram. This melting point of BaTiO_3 can be reduced to a eutectic point of $\sim 1320^\circ\text{C}$ if the BaTiO_3 is TiO_2 -rich [11]. Highly oxygen-deficient, non-stoichiometric BaTiO_3 grains may also exhibit a significantly low melting temperature that is even lower than that of nickel. Further investigation and experiment evidence are needed to determine whether slow degradation failures can reach such a high local temperature.

Based on the FA results, the failure mechanism in BME capacitors with a BaTiO_3 dielectric might be better described by a two-stage dielectric wearout that initiated with a slow dielectric degradation, characterized by a gradual leakage current increase against stress time, followed by a thermally dominated catastrophic breakdown (either ABD or TRA). When the failure criterion is set with respect to a leakage current level ($100\mu\text{A}$ in this study), some BME capacitors will reach the failure level with a catastrophic failure, and some will fail prior to the occurrence of a catastrophic breakdown. This modified two-stage dielectric breakdown model for BME capacitors with X7R dielectrics is illustrated in Figure 20.

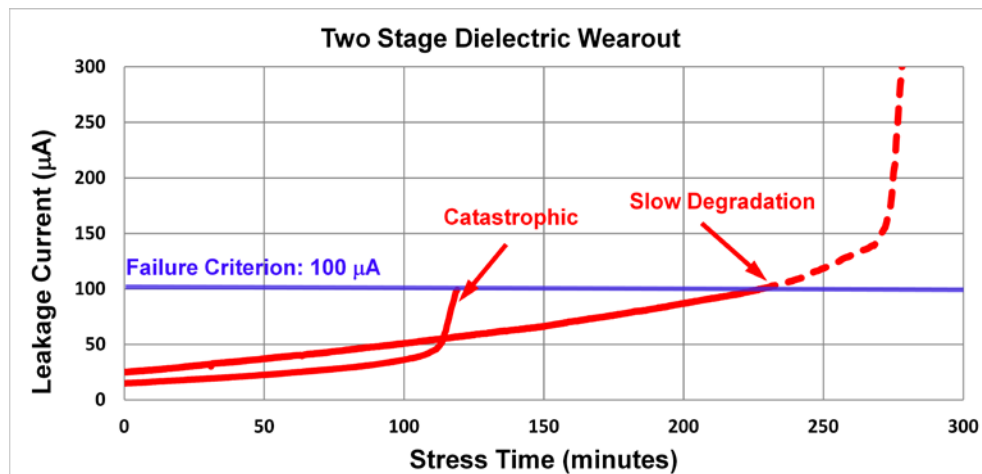


Figure 20. Two-stage dielectric wearout failure modes is proposed for describe the dielectric breakdown behaviors in BME capacitors.

Summary

FA results of four BME capacitors that failed with three different failure modes were presented and discussed. The following conclusions are based on the findings:

The failure analysis indicates that the failure modes in BME capacitors with BaTiO_3 dielectrics can be more accurately described as a two-stage dielectric wearout that begins with a slow dielectric degradation, characterized by a gradual leakage current increase with stress time, followed by a thermally dominated catastrophic breakdown (either ABD or TRA).

All samples that failed with ABD and TRA had similar damage characteristics: an incompletely burned carbon binder particle, adjacent to significant transverse cracks. However, the damage site in ABD failures is larger than that in TRA failures. The similarity in the physical characteristics for ABD and TRA failures indicates that there is no fundamental physical difference between ABD and TRA for BME capacitors. The failure mode in these BME capacitors is a combination of ABD and TRA and is “catastrophic” in general.

The FA on the sample that failed with a slow degradation suggests the following failure process: With a gradual increase of leakage current, the electromigration of oxygen vacancies changes the initial stoichiometry of BaTiO_3 grains and causes the local hollowing and melting of dielectric grains, as well as the formation of cracks. The molten dielectric dissolves the internal nickel electrodes and behaves like a vehicle to transport the nickel along the transverse cracks and results in the resistive short. This study indicates that there was no nickel migration in the BME capacitors, even under highly accelerated life stress conditions. Some BME capacitors with slow degradation

will reach the failure level with a catastrophic failure, and some will fail prior to the occurrence of a catastrophic breakdown. The failure process involves a localized high temperature that can melt both dielectric and nickel.

Significant amount of cracks are revealed for every failed BME capacitor, regardless of the failure modes. The cracks can be divided into two groups: cracks with dielectric degradation, and regular stress cracks. Since no any type of cracks was revealed during the construction analysis of fresh units, the observed cracks are the consequence of the failure, not the root cause.

Acknowledgements

The authors are thankful to the NASA Electronic Parts and Packaging (NEPP) Program Managers, Michael Sampson and Ken LaBel, for their support and encouragement. The authors also express their gratitude to Michael Sampson and Bruce Meinhold for reviewing the manuscript. The authors are also thankful to the GSFC Code 562 Parts Analysis Laboratory for technical support.

References:

1. D. Liu, "Highly Accelerated Life Stress Testing (HALST) of Base-Metal Electrode Multilayer Ceramic Capacitors," *CARTS proceeding*, pp. 235, (2013)
2. B. Rawal and N. Chan, "Conduction and Failure Mechanisms in Barium Titanate Based Ceramic Under Highly Accelerated Conditions," *Proceeding of Electronic Components Conference*, New Orleans, pp. 184, (1984)
3. J.F. Scott, B. Melnick, L. McMillan, and C. Paz de Araujo, "Dielectric Breakdown in High- ϵ Films for USLI DRAMs," *Integrated Ferroelectrics*, **3**, pp. 225, (1993)
4. M.J. Cozzolino, "Electrical Shorting in Multilayer Ceramic Capacitors," *CARTS proceeding*, pp. 57, (2004)
5. G.Y. Yang, E.C. Dickey, C.A. Randall, etc., "Oxygen Nonstoichiometry and Dielectric Evolution of BaTiO₃. Part I---Improvement of Insulating Resistance with Reoxidation," *J. Appl. Phys.* **96** [12], pp. 7492, (2004)
6. G.Y. Yang, E.C. Dickey, C.A. Randall, etc., "Oxygen Nonstoichiometry and Dielectric Evolution of BaTiO₃. Part II---Insulation Resistance Degradation Under Applied DC Bias," *J. Appl. Phys.* **96** [12], pp. 7500, (2004)
7. D. Liu and M. Sampson, "Some Aspects of the Failure Mechanisms in BaTiO₃-Based Multilayer Ceramic Capacitors," *CARTS proceedings*, pp. 59, (2012)
8. J. O'Dwyer, *The Theory of Dielectric Breakdown of Solids* (Charendon Press, Oxford, 1964)
9. R. Degraeve, J. Ogier, R. Bellens, P. Roussel, and G. Groeseneken, "A New Model for the Field Dependence of Intrinsic and Extrinsic Time-Dependent Dielectric Breakdown," *IEEE Transactions on Electron Devices*, **45** [2], pp. 472 (1998)
10. D. Liu and M. Sampson, "Reliability Evaluation of Base-Metal-Electrode Multilayer Ceramic Capacitors for Potential Space Applications," *CARTS proceedings*, pp. 45, (2011)
11. R.S. Roth, *Phase Diagrams for Electronic Ceramics I*: (American Ceramics Society, 2003)